

Determination of Effective Magnetization and Gyromagnetic Ratio of Yttrium Iron Garnet From Multi-Mode Ferromagnetic Resonance S_{21} Spectra

Kevin J. Coakley¹, Pavel Kabos¹, and Scooter D. Johnson²

¹National Institute of Standards and Technology, Boulder, CO 80305 USA

²U.S. Naval Research Laboratory, Washington, DC 20375 USA

We acquire ferromagnetic resonance (FMR) spectra for an out-of-plane magnetized yttrium iron garnet sample with a vector network analyzer at microwave frequencies ranging from 4.2 to 5.2 GHz. The applied static magnetic field varies from approximately 253.6 to 260.1 kA/m. Based on an empirical model for resonant features in the S_{21} spectrum produced by the excitation of multiple modes and instrumental effects, we predict measured values of S_{21} -parameters. For each of many microwave frequencies, for each of multiple modes, we determine the resonant field value of the applied magnetic field, an amplitude, and an FMR linewidth. Based on the frequency-dependent resonant field values produced by excitation of the main mode, we determine the effective magnetization and the gyromagnetic ratio of the sample.

Index Terms—Effective magnetization, empirical modeling, ferromagnetic resonance (FMR) spectra, statistical methods.

I. INTRODUCTION

ONE of the recent and widely used standard techniques in the broadband characterization of magnetic materials by ferromagnetic resonance (FMR) is to position the investigated material over a stripline or coplanar waveguide (CPW). Because the technique is non-resonant, it enables the measurement of magnetic excitations in the investigated specimen over a broad frequency range. For a comparison of the most common techniques, see [1] and [2]. Here, we will focus on vector network analyzer (VNA) measurements. The advantage of the VNA approach is its full amplitude and phase characterization capabilities. The FMR parameters are obtained from standard scattering S-parameters as a function of the frequency and applied magnetic field where the field is fixed and the frequency varied (swept) as in [1] and [2], or the frequency is fixed and the applied magnetic field is swept (for example, see [3]). A typical measurement setup utilizes a CPW that operates over a broad frequency range—typically 1–40 GHz. A sample is mounted in a “flip-chip” setup in close proximity to the conductor line so that the material undergoes FMR at the selected field and frequency. The resulting absorption is detected by the VNA. For the analysis of a single-resonance mode based on frequency-swept VNA-FMR measurements, see [1] and [2]. The procedure for subtracting the background from field swept VNA-FMR measurement is presented in [4]. The abovementioned examples are for the case where the analyzed FMR spectrum corresponds to a single uniform mode excitation. For this case, the field sweep can be designed so that the measured spectra correspond to either a uniform pre-

cession mode for a sample with a large linewidth mode or for a large area sample. Usually, only the uniform precession mode is observed. In contrast, very low-loss materials, such as yttrium iron garnet (YIG), may yield a more complicated FMR signal. For instance, broad frequency or field sweeps, particularly in dimensionally restricted samples, such as thin-film magnetostatic mode YIG waveguides [5]–[7], patterned YIG [8], 2-D magnonic crystals [9], patterned multilayer structures [10], and magnetic nanowires [11], excite a large number of modes and produce multi-mode FMR spectra. The degree of separation of features in such multi-mode FMR spectra depends on the film dimensions. For example, as the thickness of a low-loss film increases but all other dimensions remain fixed, the separation between resonant values of the applied field decreases. The applications of YIG films and spheres are well-established and growing. Potential new application areas include spin-based electronics and quantum computing. Unfortunately, in contrast to the well-established characterization of measured single-mode excitation spectra discussed in the above references, there is almost no effort to characterize magnetic material properties based on multi-mode FMR spectra. This study utilizes the VNA techniques in a field-swept configuration with the sample surface normal vector oriented parallel to the applied field, referred to herein as the out-of-plane (OOP) orientation. Measurements in this study were taken with a CPW with metal backing. The signal line was 50 μm wide with no spacer between the waveguide and the sample. To provide an adequate ground connection, the top-side ground plane was electrically connected to the backside ground plane with an array of vias that extended along the path of the conductor. This configuration ensured a good response up to 40 GHz. The VNA was calibrated by a standard short-open-load-through method [12] out to the end of the coaxial cables. The VNA power was fixed at 0 dBm. At each fixed frequency, measurements were acquired as a function of the bias magnetic field with LabVIEW [13]

Manuscript received September 24, 2020; revised November 30, 2020; accepted March 7, 2021. Date of publication March 12, 2021; date of current version April 19, 2021. Corresponding author: K. J. Coakley (e-mail: kevin.coakley@nist.gov).

Color versions of one or more figures in this article are available at <https://doi.org/10.1109/TMAG.2021.3065758>.

Digital Object Identifier 10.1109/TMAG.2021.3065758

U.S. Government work not protected by U.S. copyright.

software. Here, we develop a method to determine relevant magnetic material parameters from multi-mode experimental spectra. As an illustration, we apply our method to VNA-FMR field-swept measurements on a magnetized OOP 5 μm thick single-crystal YIG 5 mm \times 5 mm square film grown on a $\text{Gd}_3\text{Ga}_5\text{O}_{12}$ (GGG) substrate by liquid phase epitaxy (LPE). The film was manufactured by [14]. We note that, in a low-loss YIG film, experimental data indicate that a mixture of magnetostatic modes and standing wave modes is excited at various depths. The proposed procedure is universal and can be also applied to frequency-swept VNA-FMR measurements of OOP magnetic materials.

II. METHODS

A. Physical Model for Magnetic Susceptibility

The magnetization dynamics are described by the Landau–Lifshitz equation (LLE) with a damping term. For an OOP magnetized film with OOP uniaxial anisotropy, the magnetic susceptibility as derived from LLE can be expressed as [3], [15]

$$\chi(H) = \frac{M_{\text{eff}}(H - M_{\text{eff}})}{\left((H - M_{\text{eff}})^2 - \left(\frac{2\pi f}{\gamma \mu_o}\right)^2\right) - i(\Delta H(H - M_{\text{eff}}))} \quad (1)$$

where $M_{\text{eff}} = M_s - H_k^\perp$, $\mu_o = 4\pi \times 10^{-7} \text{ N/A}^2$ is the vacuum magnetic permeability, M_s is the saturation magnetization, H_k^\perp is the OOP anisotropy field, ΔH is the linewidth, H is the applied magnetic field, f is frequency, $\gamma = g\mu_B/\hbar = 1.760859770 \times 10^{11} \text{ s}^{-1}\text{T}^{-1}$ is the gyromagnetic ratio of the free electron, g is the Landé spectroscopic splitting factor, μ_B is the Bohr magneton, and \hbar is the reduced Planck constant. In this work, we express all quantities in SI units. In our analysis of the S_{21} spectrum due to multi-mode excitations, we make the *ad hoc* assumption that each of the resonant features can be modeled similar to how the susceptibility of the uniform precession mode is modeled by (1). Each resonant feature is characterized by an amplitude, resonant field, and linewidth. According to Kittel's equation for an OOP magnetized film, the resonant field value for the main mode, H_{r*} , varies with frequency as

$$H_{r*} = M_{\text{eff}} + \frac{2\pi f}{\gamma \mu_o}. \quad (2)$$

Rewriting (2) and assuming that $M_{\text{eff}} = M_s$

$$M_s = H_{r*} - \frac{2\pi f}{\gamma \mu_o}. \quad (3)$$

B. Empirical Prediction Model for S_{21}

Here, we measure S_{21} scattering parameters with a VNA with methods similar to those described in [1] and [2]. We model the contribution of each excited mode to the theoretical S_{21} spectrum with a generalization of (1). For each

excited mode, we define an empirical prediction term S as

$$S(H) = \tilde{A} \left(H - H_r + \frac{2\pi f}{\gamma \mu_o} \right) \left[\left(H - H_r + \frac{2\pi f}{\gamma \mu_o} \right)^2 - \left(\frac{2\pi f}{\gamma \mu_o} \right)^2 + i\kappa \left(\Delta H \left(H - H_r + \frac{2\pi f}{\gamma \mu_o} \right) \right] \quad (4)$$

where H_r and \tilde{A} are the resonant field value and amplitude of the feature generated by a mode, and κ is equal to either -1 or 1 (for all modes).

The real and imaginary parts of S are

$$\text{Re}(S(H)) = \frac{\tilde{A}}{D} \left(H - H_r + \frac{2\pi f}{\gamma \mu_o} \right) \times \left(\left(H - H_r + \frac{2\pi f}{\gamma \mu_o} \right)^2 - \left(\frac{2\pi f}{\gamma \mu_o} \right)^2 \right) \quad (5)$$

and

$$\text{Im}(S(H)) = -\frac{\tilde{A}\kappa}{D} \Delta H \left(H - H_r + \frac{2\pi f}{\gamma \mu_o} \right)^2 \quad (6)$$

where

$$D = \left(\left(H - H_r + \frac{2\pi f}{\gamma \mu_o} \right)^2 - \left(\frac{2\pi f}{\gamma \mu_o} \right)^2 \right)^2 + \left(\Delta H \left(H - H_r + \frac{2\pi f}{\gamma \mu_o} \right) \right)^2. \quad (7)$$

At $H = H_r$, $\text{Re}(S) = 0$, and $\text{Im}(S)$ takes its maximum or minimum value depending on the signs of κ and \tilde{A} . For a model with K modes, the overall value of S is

$$S(H) = \sum_{k=1}^K S_k(H) \quad (8)$$

where S_k is the theoretical contribution due to the k th mode. The contribution of each distinct mode to S depends on three model parameters: \tilde{A} , H_r , and ΔH that, in general, vary from mode-to-mode.

Given S , we model the theoretical value of S_{21} as

$$S_{21}(H) = B(H) + \exp(i\phi)S(H) \quad (9)$$

where the phase parameter falls in the interval $[0, 2\pi]$, and the theoretical background, $B(H)$, is a linear function of H . That is

$$B(H) = \alpha + \beta H \quad (10)$$

where α and β are complex constants to be determined. Given that $(\text{Re}(\alpha), \text{Im}(\alpha)) = (\alpha_r, \alpha_i)$ and $(\text{Re}(\beta), \text{Im}(\beta)) = (\beta_r, \beta_i)$, we have that

$$\begin{aligned} \text{Re}(S_{21}(H)) &= \alpha_r + \beta_r H \\ &+ \sum_{k=1}^K (\cos(\phi) \text{Re}(S_k(H)) - \sin(\phi) \text{Im}(S_k(H))) \end{aligned} \quad (11)$$

and

$$\begin{aligned} \text{Im}(S_{21}(H)) &= \alpha_i + \beta_i H \\ &+ \sum_{k=1}^K (\sin(\phi) \text{Re}(S_k(H)) + \cos(\phi) \text{Im}(S_k(H))) \end{aligned} \quad (12)$$

where K is the number of modes in our model.

In general, a feature in the FMR spectrum could be due to a single mode or multiple modes that closely overlap. Here, we model each feature as due to a single mode. If there are K modes in the model fit to data, we refer to such a model as a K -feature model.

C. Estimation of Model Parameters

For each feature, we must estimate three model parameters: \tilde{A} , H_r , and ΔH that, in general, vary from feature-to-feature. We must also estimate a phase ϕ and four background parameters α_r , α_i , β_r , and β_i . Hence, for a model with K features, the total number of model parameters is $3K+5$. We denote these parameters as a $(3K+5)$ -dimensional vector θ . We determine θ with a two-stage stochastic optimization method. In this approach, we seek to minimize the mean-square-deviation between predicted and observed pooled spectra (from both the real and imaginary parts of S_{21}) with a modified Levenberg–Marquardt [16] method where we specify a lower and upper bound for each model parameter estimate. In stage 1, we simulate N_{sim} random realizations of θ . Each random initial parameter value is sampled from a Gaussian distribution with a mean equal to the average of its lower and upper bounds and a standard deviation equal to one-tenth of the difference of its upper and lower bounds. For each simulated initial value of θ , we determine a final estimate (and the associated value of the cost function) with the Levenberg–Marquardt method. We select the estimate that yields the lowest value of the cost function.

In stage 2, we simulate N_{sim} random initial estimates of θ , such as in stage 1, but with one major difference. In stage 2, the central value of the sampling distribution is the estimate determined in the first stage rather than the average of the upper and lower bounds. If a simulated value of a model parameter falls outside its allowed interval, we set it to the corresponding central value in the simulation model. Like in stage 1, we determine a final estimate and associated cost function for each of N_{sim} simulated initial values of θ with the Levenberg–Marquardt method and select the one that yields the lowest value of the cost function. The selected value from the stage 2 analysis is the final estimate. The primary results reported here correspond to $N_{\text{sim}} = 2000$.

Each stage of our procedure is an example of a multi-start [17] method for avoiding getting stuck in a local minimum of the cost function (see the Appendix for more details).

III. RESULTS

A. Analysis for Each Frequency

We analyze FMR spectra at microwave frequencies that range from 4.2 to 5.2 GHz. At each frequency, the strength

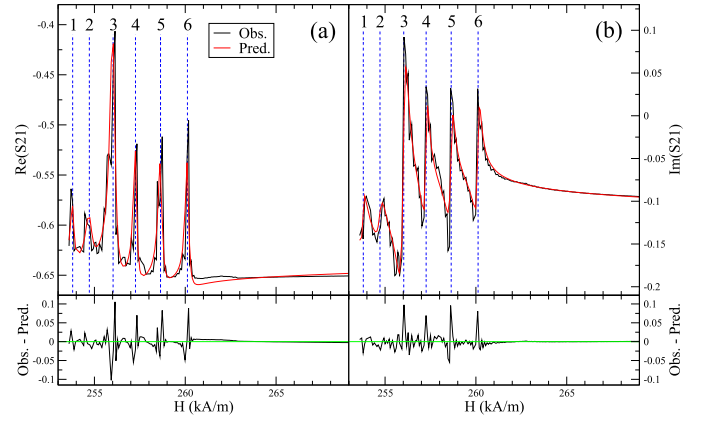


Fig. 1. Top: observed and predicted values of (a) real and (b) imaginary parts of S_{21} at $f = 4.2$ GHz. Dashed vertical lines show estimated locations of resonant values of the applied field for each of the six features. Bottom: Residuals. In our analysis, we set γ to the gyromagnetic ratio of the free electron ($1.760\,859\,770 \times 10^{11} \text{ s}^{-1}\text{T}^{-1}$).

TABLE I

SIX-FEATURE MODEL RESULTS FOR $f = 4.2$ GHz CASE. WE SET THE GYROMAGNETIC RATIO FOR THE SAMPLE TO THE GYROMAGNETIC RATIO OF THE FREE ELECTRON. THE ESTIMATES OF α_r AND α_i ARE -0.766 AND 0.048 , RESPECTIVELY. THE ESTIMATES OF β_r AND β_i (IN UNITS OF METERS/KILOAMPERES) ARE 3.57×10^{-5} AND -4.51×10^{-5} . THE ESTIMATED VALUE OF ϕ IS 109.55°

feature	\tilde{A} (A/m)	H_r (kA/m)	ΔH (kA/m)	range of predicted $\text{Re}(S)$
1	13.51	253.800	0.237	0.054
2	19.86	254.719	0.426	0.046
3	84.08	256.027	0.339	0.241
4	29.45	257.259	0.223	0.130
5	32.50	258.638	0.272	0.114
6	29.11	260.119	0.236	0.123

of the applied magnetic field H varies from approximately 253.6 to 269.1 kA/m.

In our primary study, at each frequency, we fit a six-feature model to observed spectra. Here, we constrain each amplitude (\tilde{A}) estimate to be non-negative, set $\kappa = 1$ in our prediction model [see (4)], and, similar to the approach in [3], set γ to the nominal value corresponding to the gyromagnetic ratio of the free electron. We stress that, when $\kappa = -1$, we obtained poor results. To illustrate our methods, we show predicted and observed S_{21} spectra and associated residuals for the 4.2 GHz frequency case in Fig. 1 and list associated model parameter estimates in Table I. In Fig. 1(a), we show estimates of the resonant field values for the six features as vertical dashed lines. For other frequencies, the visual agreement between observed and predicted spectra is similar to the visual agreement for the 4.2 GHz case (see Fig. 2). The root-mean-square (rms) deviation between observed and predicted spectra varied from 0.0178 to 0.0224 for the seven frequencies of interest (see Table II).

B. Determination of M_{eff} and γ

We identify the feature produced by the main mode as the one with the largest range (maximum minus minimum) of

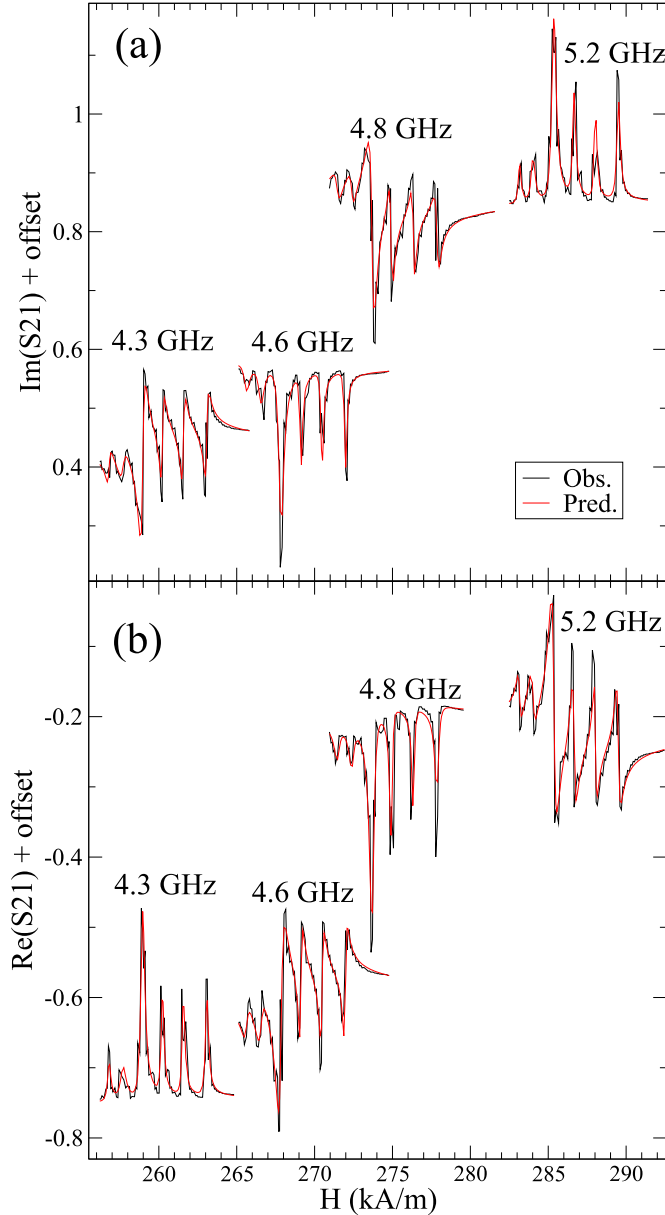


Fig. 2. Predicted (red lines) and observed (black lines) for S_{21} spectra at $f = (4.3, 4.6, 4.8 \text{ and } 5.2) \text{ GHz}$. The median values of the measured real and imaginary parts of the S_{21} spectrum at $f = (4.3, 4.6, 4.8 \text{ and } 5.2) \text{ GHz}$ are $(-0.600, 0.222, 0.626, -0.199)$ and $(0.234, 0.600, 0.118, -0.605)$, respectively. Here, to facilitate visual inspection of results, we show spectra that are translated vertically by a frequency-dependent offset that, for any frequency, varies for the real and imaginary parts of S_{21} . The value of γ is set to the same value as in analysis in Fig. 1.

predicted values of $\text{Re}(S)$ [see (5)] over all values of H in the analyzed FMR spectrum (see Table I and Figs. 1 and 2). For each frequency, this selection rule identifies the third feature as that produced by the main mode. For the measurements studied here, the estimated amplitude associated with the selected feature is larger than the amplitudes associated with the non-selected features (see Table I). Based on (2), we model our estimate of the resonant field value associated with the main mode at f as $\hat{H}_{r*}(f)$ where

$$\hat{H}_{r*}(f) = M_{\text{eff}} + \frac{2\pi f}{\gamma \mu_0} + \epsilon(f) \quad (13)$$

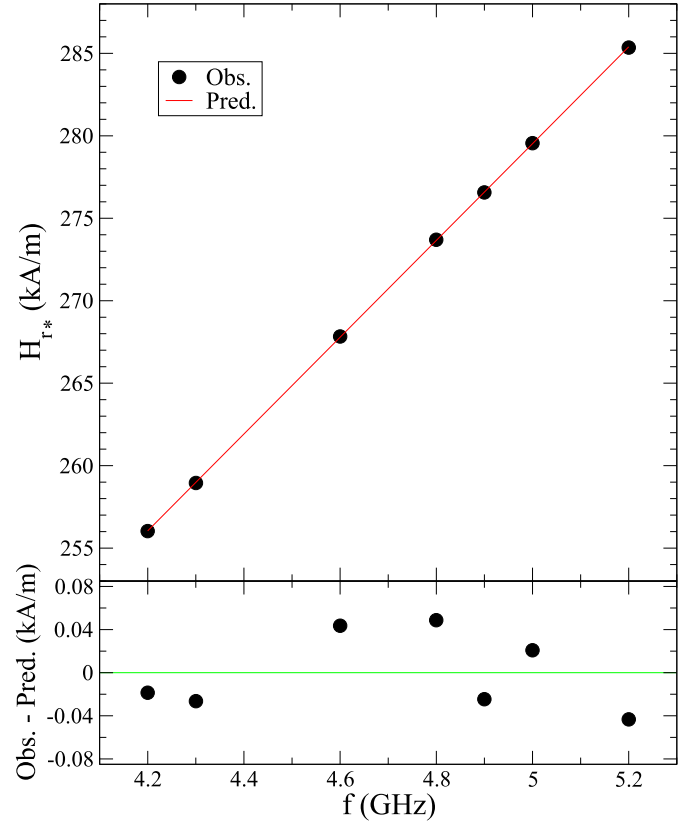


Fig. 3. Top: estimated resonant field values of the main mode versus microwave frequency (see Table II) and predicted values based on fitting the model [see (13)] to observed data by the method of ordinary least squares. Our estimates of M_{eff} and γ are $132.79(0.52) \text{ kA/m}$ and $1.7037(0.0065) \times 10^{11} \text{ s}^{-1}\text{T}^{-1}$. Bottom: residuals.

TABLE II

SIX-FEATURE MODEL RESULTS FOR MAIN MODE (THIRD) FEATURE FOR ALL f VALUES. WE SET THE GYROMAGNETIC RATIO FOR THE SAMPLE TO THE GYROMAGNETIC RATIO OF THE FREE ELECTRON

f (GHz)	A (A/m)	H_r (kA/m)	ΔH (kA/m)	RMS
4.2	84.08	256.027	0.339	0.0178
4.3	83.38	258.954	0.310	0.0182
4.6	106.18	267.828	0.390	0.0195
4.8	104.31	273.703	0.351	0.0224
4.9	111.14	276.564	0.364	0.0219
5.0	99.87	279.545	0.327	0.0206
5.2	107.17	285.350	0.341	0.0210

where $\epsilon(f)$ is measurement error and M_{eff} and γ^{-1} are theoretical parameters that we determine by ordinary least squares with the \mathbf{R} [19] function `lm` (see Fig. 3). In this linear regression approach, γ^{-1} and M_{eff} are slope and intercept parameters. Our estimate of γ is the reciprocal of our estimate of γ^{-1} . Given the uncertainty of estimated γ^{-1} reported by the statistical software, we determine the uncertainty of estimated γ by the propagation of uncertainty method [21]. Our estimates of M_{eff} and γ are $132.79(0.21) \text{ kA/m}$ and $1.7037(0.0026) \times 10^{11} \text{ s}^{-1}\text{T}^{-1}$, respectively. The estimates and uncertainties (in parentheses) are determined under the assumption that the model is valid and random measurement errors at different frequencies have the same variance and are uncorrelated. The statistical software reports the standard

deviation of the random measurement error of H_{r*} at each frequency to be 0.041 kA/m based on the standard linear regression theory [18].

We cannot rule out the possibility that measured values of the resonant field for the main mode at different frequencies are affected by frequency-dependent systematic errors. We quantify additional components of uncertainty that account for this possible systematic effect on estimates of M_{eff} and γ . We split the data shown in the upper frame of Fig. 3 into two subsets. One corresponds to $f \leq 4.6$ GHz; the other corresponds to $f \geq 4.8$ GHz. For each subset, we determine estimates of M_{eff} and γ . For the two subsets, the magnitudes of the difference in the estimates of M_{eff} and γ are 1.66 kA/m and $2.06 \times 10^9 \text{ s}^{-1}\text{T}^{-1}$, respectively. For each model parameter, following [21], we quantify an additional component of uncertainty to be the standard deviation of a uniform distribution that has width equal to the magnitude of the relevant difference of estimates for the two subsets. The additional uncertainty components for M_{eff} and γ are 0.48 kA/m and $5.9 \times 10^8 \text{ s}^{-1}\text{T}^{-1}$. Thus, the combined uncertainties of our estimates due to random effects and the systematic effect are 0.52 kA/m and $6.5 \times 10^8 \text{ s}^{-1}\text{T}^{-1}$. As a caveat, other systematic effects may influence our estimates of M_{eff} and γ .

C. Discussion

1) *Amplitude Constraint*: As discussed earlier, in our primary study, we constrain the amplitude estimates to be non-negative. In a secondary study, we removed this constraint and allowed amplitude estimates to be positive or non-positive. In this secondary study, at each frequency, the signs of the estimated amplitudes were the same for all six features. However, the signs varied from frequency to frequency. Nonetheless, for each frequency, the difference in the magnitude of the estimated amplitude for any particular feature determined in the two studies was negligible. Moreover, at any frequency, the difference between predicted FMR spectra was negligible. We attribute discrepancies in the signs to the fact that, if the phase ϕ in our model [see (9)] is shifted by π and the estimated amplitudes are scaled by -1 , both $\exp(i\phi)$ and $S(H)$ will change sign, but their product will not.

2) *Choice of N_{sim}* : We set γ to its nominal value and obtained results for $N_{\text{sim}} = 1000, 2000, 4000$, and 8000 . For each frequency, the rms deviations between observed and predicted S_{21} spectra determined for the different choices of N_{sim} agreed to within $1.2 \times 10^{-11}\%$ or less. Relative to the $N_{\text{sim}} = 2000$ case, the difference between estimated M_{eff} determined for $N_{\text{sim}} = (1000, 4000, 8000)$ are $(-2.3, -5.9, -8.1) \times 10^{-6}$ kA/m. The differences between γ estimates are $(-4.0, -7.3, -11.1) \times 10^3 \text{ s}^{-1}\text{T}^{-1}$. Relative to reported uncertainties for M_{eff} and γ (0.52 kA/m and $6.5 \times 10^8 \text{ s}^{-1}\text{T}^{-1}$), these differences are negligible.

3) *Choice of γ* : As a consistency check, we determined the resonant field values for the seven frequencies for the case where γ equals the empirical estimated reported in Section III-B. The resulting differences in the estimated resonant field values ranged from -7.5×10^{-6} kA/m to

-2.5×10^{-6} kA/m. The differences in the empirical estimates of M_{eff} and γ determined by fitting the model [see (13)] to the updated resonant field values, relative to our primary study result, -8.1×10^{-6} kA/m and $-4.1 \times 10^3 \text{ s}^{-1}\text{T}^{-1}$, are negligible relative to reported uncertainties.

4) *Model Choice*: We fit a five-feature model to the same spectra as previously analyzed and determined model parameters for features 2, 3, 4, 5, and 6. The estimates of the resonant field values for the main mode for the seven frequencies increased, on average, by 0.011 kA/m. However, the differences between the estimates of M_{eff} and γ determined by the five- and six-feature models, 0.0074 kA/m and $-3.4 \times 10^6 \text{ s}^{-1}\text{T}^{-1}$, are negligible relative to reported uncertainties.

5) *Random Uncertainty of Measured H_{r*}* : In Section III-B, we determined the random uncertainty of measured H_{r*} at each frequency to be 0.041 kA/m. Based on the assumption that random measurement errors have the same standard deviation and are uncorrelated, the statistical software that implemented the Levenberg–Marquardt method reported random uncertainties for measured H_{r*} at each frequency that ranged from 0.010 to 0.012 kA/m. A possible explanation for the discrepancy between these uncertainties and the reported uncertainty in Section III-B is a violation of the modeling assumption that additive measurement errors have the same standard deviation. This hypothesis is supported by the residual plot in Fig. 1(b). The analysis of multiple (at least 20) spectra at each frequency may be required to fully understand this discrepancy. Because of this discrepancy, we do not report uncertainties for any of the estimated model parameters listed in Tables I and II.

6) *Application to Other Experimental Data*: We anticipate that our method will perform well for multi-mode FMR spectra with more features (say up to 20) that are as well-separated as those in this study. How well our method works for features that are not well-separated is a subject for further study. In this study, we determined the number of features by scientific judgment. In more complicated cases where features are not as well-separated as in this study, it may be helpful to select the number of features by statistical learning methods, such as cross-validation [22], [23]. In other studies, features of interest in multi-mode FMR spectra might not be as well-separated as in this study. For more complicated cases, a more complicated stochastic optimization method may be required.

IV. CONCLUSION

For a YIG sample, we determined a resonant field value, linewidth, and amplitude for each of many features produced by a multi-mode excitation. Based on the analysis of the main feature for microwave frequencies ranging from 4.2 to 5.2 GHz, we determined the effective magnetization and gyromagnetic ratio of the YIG sample.

APPENDIX

MODEL PARAMETER ESTIMATION METHOD

For a model with K features, we estimate a $(3K+5)$ -dimensional model parameter vector θ by minimizing

the following cost function:

$$C = \sum_j (\epsilon_{\text{Re}}^2(j) + \epsilon_{\text{Im}}^2(j))$$

where $\epsilon_{\text{Re}}(j)$ is the difference between the observed and predicted values of the real part of S_{21} at $H = H_j$ [see (5)], and $\epsilon_{\text{Im}}(j)$ is the difference between the observed and predicted values of the imaginary part of S_{21} at $H = H_j$ [see (6)].

As described in Section II-C, for each of many randomly general initial values of our model parameter vector θ , we determine an approximate global minimum of C with a modified Levenberg–Marquardt [16] method where we specify lower and upper bounds for each component of θ . We implement our optimization with public domain **R** [19] software. In particular, we call the function **nls.lm** from the package **minpack.lm** [20].

The lower and upper bounds for each linewidth parameter ΔH are 0.008 and 0.8 kA/m. The lower and upper bounds for each resonant field value H_r are centered about an initial estimate \tilde{H}_r determined from a peak finding analysis of the spectra. For each feature, we set \tilde{H}_r to the location of a local extremum of the imaginary part of S_{21} . For example, for the 4.2 GHz case, we set initial estimates to the locations of local maxima of the imaginary part of S_{21} . For each feature, the search interval is $[\tilde{H}_r - 0.8, \tilde{H}_r + 0.8]$ kA/m. For the angle ϕ , the bounds are 0 and 2π . For α_r and α_i , the bounds are -2 and 2 , respectively. For β_r and β_i , the bounds are -0.0126 and 0.0126 m/kA, respectively. The lower and upper bounds on estimates of \tilde{A} are 0 and 8 kA/m, respectively, in our primary analysis.

ACKNOWLEDGMENT

The authors thank J. Splett and H. Nembach of the National Institute of Standards and Technology (NIST) for helpful comments. Contributions by the staff of NIST, an agency of the U.S. Government, are not subject to copyright in the U.S. Certain commercial products or company names are identified here to describe our study adequately. Such identification is not intended to imply recommendation or endorsement by the NIST nor is it intended to imply that the products or names identified are necessarily the best available for the purpose.

REFERENCES

- [1] S. S. Kalarickal *et al.*, “Ferromagnetic resonance linewidth in metallic thin films: Comparison of measurement methods,” *J. Appl. Phys.*, vol. 99, no. 9, May 2006, Art. no. 093909.
- [2] C. Bilzer, T. Devolder, P. Crozat, C. Chappert, S. Cardoso, and P. P. Freitas, “Vector network analyzer ferromagnetic resonance of thin films on coplanar waveguides: Comparison of different evaluation methods,” *J. Appl. Phys.*, vol. 101, no. 7, Apr. 2007, Art. no. 074505.
- [3] H. Nembach *et al.*, “Perpendicular ferromagnetic resonance measurements of damping and Landé g -factor in sputtered $(\text{Co}_2\text{Mn})_{1-x}\text{Ge}_x$ thin films,” *Phys. Rev. B, Condens. Matter*, vol. 84, Aug. 2011, Art. no. 054424.
- [4] A. J. Berger, E. R. Edwards, H. T. Nembach, A. D. Karenowska, M. Weiler, and T. J. Silva, “Inductive detection of fieldlike and damping-like ac inverse spin-orbit torques in ferromagnet/normal-metal bilayers,” *Phys. Rev. B, Condens. Matter*, vol. 97, Mar. 2018, Art. no. 094407.
- [5] J. D. Adam, S. H. Talisa, and J. A. Keresztes, “Non-destructive evaluation of YIG films by ferromagnetic resonance,” *IEEE Trans. Magn.*, vol. 25, no. 5, pp. 3488–3490, Sep. 1989.
- [6] C. W. Sandweg, Y. Kajiwar, K. Ando, E. Saitoh, and B. Hillebrands, “Enhancement of the spin pumping efficiency by spin wave mode selection,” *Appl. Phys. Lett.*, vol. 97, no. 25, Dec. 2010, Art. no. 252504.
- [7] S. Klingler *et al.*, “Measurements of the exchange stiffness of YIG films using broadband ferromagnetic resonance techniques,” *J. Phys. D, Appl. Phys.*, vol. 48, no. 1, Jan. 2015, Art. no. 015001.
- [8] E. R. J. Edwards, M. Buchmeier, V. E. Demidov, and S. O. Demokritov, “Magnetostatic spin-wave modes of an in-plane magnetized garnet-film disk,” *J. Appl. Phys.*, vol. 113, no. 10, Mar. 2013, Art. no. 103901.
- [9] A. Manzin, G. Barrera, F. Celegato, M. Coisson, and P. Tiberto, “Influence of lattice defects on the ferromagnetic resonance behaviour of 2D magnonic crystals,” *Sci. Rep.*, vol. 6, p. 22004, Feb. 2016.
- [10] G. De Loubens, V. Naletov, O. Klein, J. B. Youssef, F. Boust, and N. Vukadinovic, “Magnetic resonance studies of the fundamental spin-wave modes in individual submicron Cu/NiFe/Cu perpendicularly magnetized disks,” *Phys. Rev. Lett.*, vol. 98, Mar. 2007, Art. no. 127601.
- [11] Y. Zhang, J. Um, W. Zhou, B. Stadler, and R. Franklin, “Magnetic nanowires for RF applications: Ferromagnetic resonance and permeability characterization,” in *IEEE MTT-S Int. Microw. Symp. Dig.*, Jun. 2019, pp. 1100–1103.
- [12] R. A. Ginley, “Establishing traceability for SOLT calibration kits,” in *Proc. 90th ARFTG Microw. Meas. Symp. (ARFTG)*, Boulder, CO, USA, Nov. 2017, pp. 1–4, doi: [10.1109/ARFTG.2017.8255871](https://doi.org/10.1109/ARFTG.2017.8255871).
- [13] C. Elliott, V. Vijayakumar, W. Zink, and R. R. Hansen, “National instruments LabVIEW: A programming environment for laboratory automation and measurement,” *J. Assoc. Lab. Automat.*, vol. 12, pp. 17–24, Feb. 2007, doi: [10.1016/j.jala.2006.07.012](https://doi.org/10.1016/j.jala.2006.07.012).
- [14] *Metamagnetics*, Flanders Road, Suite, Westborough, MA, USA.
- [15] I. S. Maksymov and M. Kostylev, “Broadband stripline ferromagnetic resonance spectroscopy of ferromagnetic films, multilayers and nanostructures,” *Phys. E, Low-Dimensional Syst. Nanostruct.*, vol. 69, pp. 253–293, May 2015.
- [16] J. J. Moré, “The Levenberg-Marquardt algorithm: Implementation and theory,” in *Numerical Analysis*. Berlin, Germany: Springer, 1978, pp. 105–116.
- [17] R. Marti, M. G. Resende, and C. C. Ribeiro, “Multi-start methods for combinatorial optimization,” *Eur. J. Oper. Res.*, vol. 226, pp. 1–8, Apr. 2013.
- [18] N. R. Draper and H. Smith, *Applied Regression Analysis*, vol. 326. Hoboken, NJ, USA: Wiley, 1998.
- [19] R Core Team. (2018). *R: A Language and Environment for Statistical Computing*, R Foundation for Statistical Computing, Vienna, Austria. [Online]. Available: <https://www.R-project.org/>
- [20] T. V. Elzhov, K. M. Mullen, A.-N. Spiess, and B. Bolker. (2016). *Minpack.lm: R Interface to the Levenberg-Marquardt Non-linear Least-Squares Algorithm Found in MINPACK, Plus Support for Bounds*, Note = R Package Version 1.2-1. [Online]. Available: <https://CRAN.R-project.org/package=minpack.lm>
- [21] N. B. Taylor and E. C. Kuyatt, “Guidelines for evaluating and expressing the uncertainty of NIST measurement results,” NIST, Gaithersburg, MD, USA, Tech. Rep. 1297, 1994.
- [22] M. Stone, “Cross-validatory choice and assessment of statistical predictions,” *J. Roy. Stat. Soc., B, Methodol.*, vol. 36, no. 2, pp. 111–133, Jan. 1974.
- [23] S. Arlot and A. Celisse, “A survey of cross-validation procedures for model selection,” *Statist. Surv.*, vol. 4, pp. 40–79, Jul. 2010.